Macromolecules
ARTICLE

Macromolecules **2010**, *43*, 5455–5469 **5455**
DOI: 10.1021/ma100677f

Crystallization and Melting Simulations of Oligomeric α1 Isotactic Polypropylene

Nikolaos A. Romanos and Doros N. Theodorou*

School of Chemical Engineering, Department of Materials Science & Engineering, National Technical University of Athens, Heroon Polytechniou 9, Zografou Campus, 157 80 Athens, Greece

Received March 29, 2010; Revised Manuscript Received May 9, 2010

ABSTRACT: The crystallization and melting of the α1 form of isotactic polypropylene (iPP) was studied with molecular dynamics (MD) simulations, using a fully flexible force field representing the C and H atoms atomistically and the CH_3 groups as united atoms. Initially, a model crystal lattice of iPP of infinite molar mass was generated from experimental diffraction data, adding the pendant and geminal hydrogens. Next, crystal configurations of finite molar mass were created from this initial model lattice, and it was verified that the force field could preserve the crystal structure, keeping intact the monoclinic symmetry of the crystal. The generated configurations were heated under isobaric conditions, until a first-order transition into the melt state took place. The density change upon melting and the enthalpy of melting were estimated as differences between well-equilibrated ensembles of crystal and melt configurations. In order to calculate the equilibrium melting temperature T_m, composite (sandwich) configurations consisting of both melt and crystal subdomains in contact with each other were generated and subjected to a series of isothermal−isobaric simulations at a variety of temperatures. T_m was determined as that temperature where none of the phases in the sandwich grew at the expense of the other. As proximity to the glass temperature T_g made the dynamics of crystal growth very sluggish, a constraining potential inducing helical conformations along the chains was introduced to accelerate crystallization. Using a novel Gibbs−Duhem integration scheme that utilizes data from both sandwich and single-phase solid and liquid simulations, results for equilibrium solid−liquid coexistence were extrapolated to zero constraining potential. An accurate estimate of T_m was thereby obtained.

I. Introduction

Semicrystalline polymers, such as polyethylene (PE), polypropylene (PP), and poly(ethylene terephthalate) (PET), play a very important role in contemporary life.[1] Their physical properties depend sensitively on their complex morphology, often characterized by a hierarchy of structures, which are shaped by their chemical constitution and the processing conditions to which they are subjected. This explains the extensive research work that has been devoted to both experimental and modeling studies of crystallization in quiescent and flowing polymer melts.[1]

In recent years, computer simulation has emerged as a promising avenue for predicting structure−property−processing−performance relations in polymers and uncovering the molecular mechanisms underlying these relations. Despite advances in computer hardware and simulation algorithms, however, the crystallization of chain molecules is still a grand challenge for molecular simulation. It involves the development of complex structures over a wide range of length scales and, more importantly, time scales, the latter exceeding by many orders of magnitude the time scales (typically microseconds) that can be accessed by conventional atomistic simulation techniques. Coarse-graining of the representation invoked in simulations could offer a way out and has been practiced fruitfully.[2−6] In general, however, coarse-graining is much less forgiving in the crystalline, than in the amorphous, phase. Molecular details exert a decisive influence on the packing of macromolecules in crystalline domains and hence on the hierarchical structures that develop upon crystallization and on the phase transitions associated with melting. Thus, detailed atomistic simulation has to be invoked at some point, if quantitative prediction of polymer crystallization phenomena is desired.

A simple problem one can pose for atomistic simulation, whose solution is a prerequisite for addressing more complex aspects of polymer crystallization, is the following: Given a molecular model for an oligomer that yields good predictions for structure, thermodynamics, and dynamics in the melt state, can one predict the melting point T_m, at which thermodynamic equilibrium is established between the solid and liquid phases of the oligomer, and the changes in thermodynamic properties upon melting? This problem has been addressed with considerable success for oligomers of polyethylene,[7,8] which crystallizes in an all-trans conformation. In this paper we try to address it for isotactic polypropylene, a polymer which crystallizes in a helical conformation and whose sluggish crystallization dynamics poses a severe challenge for molecular simulation.

Isotactic polypropylene is composed of a racemic mixture of chiral chains;[9] it contains left-handed and right-handed helices coexisting in equal numbers in its crystalline form. Its properties are greatly affected by the crystallization process, which can produce four different crystal forms:[10] α, β, γ, and a smectic one, which is a combination of the other three. All these various forms (phases) exist due to the different ways of packing the chiral chains. All forms exhibit a 3-folded (3_1−3 monomer units per turn) helical structure with standard repeat distance (identity period) of 0.65 nm. The α form can be distinguished further into the α1 and α2 forms, with the latter being the more stable of the two. Here we focus on the α1 structure, which is the simpler of the

*To whom correspondence should be addressed: Tel +30 210 772 3157, Fax +30 210 772 3112, e-mail doros@central.ntua.gr.

Published on Web 05/19/2010

two, containing chains only in the "down" configuration.[10,11] How this complex crystal structure is formed during crystallization from the melt is still a puzzle to researchers after more than 50 years, even though extensive studies have been reported.[10,6]

In this paper we present results from atomistic MD simulations aimed at studying the properties of iPP in both the melt and in the α1 crystal states, as well as in biphasic systems composed of these two states, using a realistic, fully flexible molecular model. We study both melting and crystallization processes, with emphasis on a reliable prediction of thermodynamic properties characteristic of solid−liquid equilibrium, namely the melting point and the enthalpy and volume of melting. Thus, our work has a different focus from the very interesting earlier simulation work of Yamamoto,[2,12] which emphasized the order−disorder transition with respect to helix handedness that precedes melting, using simplified models. To our knowledge, it is the first time that solid−liquid equilibrium is explored quantitatively with atomistic simulations for a molecule exhibiting helical conformations in the crystalline state. In order to overcome the challenge of the time scales of the crystallization process, which are enormous for this polymer in relation to the times that can be addressed by conventional MD, we introduce a novel bias method. In this method, a constraining force field is applied on all backbone carbon atoms, encouraging the adoption of helical conformations. The equilibrium melting point is computed at high values of the field, for which solid−liquid equilibrium is readily established. Then, the melting point is computed at progressively lower values of the field via Gibbs−Duhem integration. Integration down to zero field value yields a realistic estimate of the melting point.

Computer time limitations force us to work with an oligomer of iPP, of degree of polymerization 17. Although higher than used in most previous simulations of crystallization and melting,[2,7,13] this chain length does not allow us to study metastable states with chain folding that are characteristic of long-chain polymer crystals. We note that such folded states have been examined in the context of coarse-grained simulations.[3,4] The work reported herein is complementary to coarse-grained simulation work, since it proposes a methodology whereby the thermodynamics of melting can be reliably predicted from a detailed molecular model of the polymer.

II. Previous Work

A. Melting. The study of polymer melting is not new. Thorough experimental investigations of melting have been conducted on alkanes[14] as well as polyethylene[15] and polypropylene.[16−18] Molecular dynamics studies of melting have been carried out on alkanes[19,20] and on polyethylene.[21] We are not aware of past atomistic simulations of melting in iPP.

B. Crystallization. The study of polymer crystallization is not new, either. One can find extensive experimental studies on iPP either of crystallization itself[22−27] or of both crystallization and melting.[28,29] Several simulation approaches have been reported, aimed at studying crystallization in polyethylene[30−35] as well as in alkanes.[36−39] Both Monte Carlo and MD simulations have been enlisted in these studies. An effective method[7] for predicting the melting point of alkanes by equating chemical potentials between the liquid and solid phases has been presented by Doye and Frenkel. In that work, an Einstein crystal is used as a reference for computing chemical potential in the solid state. An atomistic Monte Carlo simulation study of the amorphous area between crystalline lamellae of isotactic polypropylene has been presented by Kuppa et al.[40] Also, there was a 2-D simulation of the crystallization of iPP which is suggested to be operative in the 3D growth front of iPP crystals.[41] Recently, we became aware of a thorough united-atom simulation work in which both nucleation and crystal growth of octane were studied.[8] Coarse-grained simulation approaches to crystallization have appeared. Of particular relevance to this work are the simulations[42] of Haliloğlu and Mattice on polypropylene crystallization, in which a second-nearest-neighbor diamond lattice model was invoked. The crystallization process not only is observed in synthetic polymeric materials but also is of interest in living organisms with applications to molecular biology, medicine, pharmacology, food chemistry, and nanoelectronics.[43−46] The similarities found between the mechanism of the crystallization of synthetic polymers and biological structures can provide insight for understanding the latter.

The theory[6] which has been developed for understanding the mechanism of the crystallization of polymers discerns many steps, of which the three most important are (i) nucleation of lamellae, (ii) increase of the thickness of the lamellae, and (iii) kinetics in the growth front. Many approaches have been proposed for a quantitative description of these steps, and long-standing debates have arisen in the field. The development of the theory of polymer crystallization will not be discussed further here. We just mention a main difference between the crystallization of small molecules and that of polymer molecules. For the latter, and for common molecular weights, the radius of gyration R_g of a polymeric molecule is larger than the critical size r_c for the growth of a crystal nucleus. As a result, one polymer molecule can participate in more than one crystal nuclei. We also mention the work[47] of Strobl, who speaks of a liquid−liquid separation preceding polymer crystallization.

In general, crystallization from the melt can be distinguished into two different processes, namely (i) nucleation and (ii) crystal growth. The computational work presented in this article focuses on growth as opposed to nucleation. It aims at developing and implementing a computational strategy, based on molecular dynamics, whereby solid−liquid equilibrium can be reliably explored with an atomistic polymer model.

III. Method

A. Construction of Unit Cell for Crystal of Infinite Molar Mass. In the present paper we deal with the α1 form of iPP. An initial set of atomic coordinates in the unit cell of iPP can be found in the original paper[48] of Natta and Corradini, who discovered iPP. In later studies[49] these coordinates were refined. It was also shown that the α form of the crystal actually consisted of α1 and α2 forms, both belonging to the monoclinic system.[50] The crystal lattice of the α1 form was found to belong to the $C2/c$ space group, with unit cell constants $a = 6.63$ Å, $b = 20.78$ Å, and $c = 6.50$ Å and angles $\alpha = \gamma = 90°$, $\beta = 99.5°$. One unit cell consists of 4 3-folded pieces of chains, each contributing 9 carbon atoms (6 skeletal carbons and 3 carbons belonging to pendant methyl groups) to the unit cell. The chain conformation for the unit cell follows the pattern Rdw, Ldw, Rdw, Ldw, with L meaning left-handedness, R meaning right-handedness, and dw being an abbreviation for the word down (Figure 1). In order to construct the unit cell with all the chains from the crystallographic data,[49] including the hydrogens connected to the backbone atoms, the following procedure was used:

(i) We start with the dimensionless coordinates (Table 1) of one of the chains in the unit cell, based on experimental diffraction data corresponding to the monoclinic system. Applying the symmetry operations (Table 2) of the crystal structure, the other chains are formed.

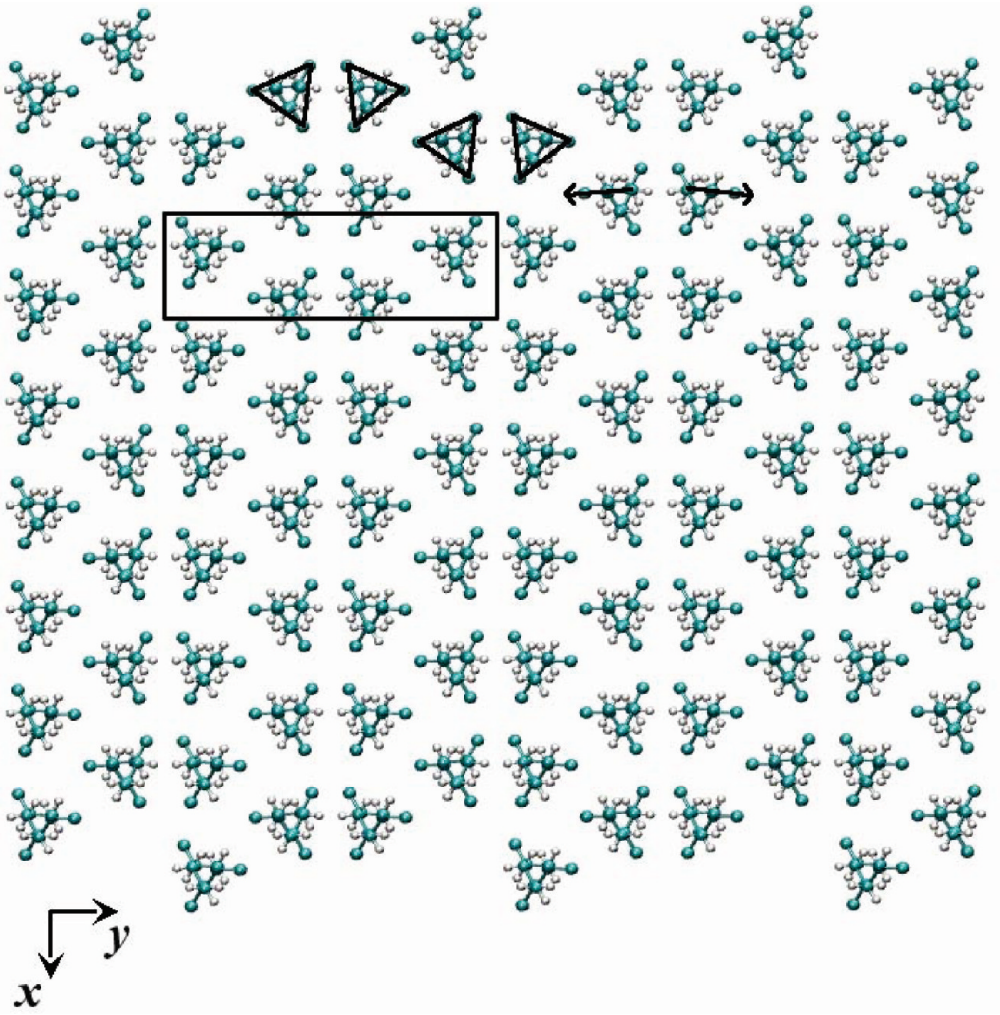

Figure 1. The 96 chain−17mer system we used for our simulations, as created from crystallographic data. The system is viewed down the **c** crystallographic axis. With triangles are shown the left and right orientations of chains (from the left-hand side of the figure, L R L R), while arrows indicate the down direction. The rectangle outlines the projection of an α1 unit cell. The *x*- and *y*-coordinate directions are shown on the left-hand side of the figure.

Table 1. Dimensionless Coordinates Used for the Formation of the α1 Crystal of iPP (Ref 49)

X	*Y*	*Z*
−0.0727	0.2291	0.2004
−0.0765	0.1592	0.2788
−0.1021	0.1602	0.5098
−0.3087	0.0589	0.4941
−0.1146	0.0928	0.6057
−0.1044	0.0854	0.8428
0.2775	0.0797	0.9260
0.0872	0.1156	0.9730
0.1026	0.1221	1.2109

(ii) Every dimensionless coordinate along each crystallographic axis is multiplied by the corresponding lattice parameter. After doing so, each coordinate is expressed as a length in the monoclinic system.

(iii) Then, a transformation from the monoclinic system to an orthonormal frame of reference takes place, taking into account that the angle between axes **a** and **c** is different from 90°. Axes *x* and *y* of the orthonormal system are taken along unit vectors **a** and **b** of the unit cell, while axis **c** of the unit cell is in the *zx* plane, but inclined by 9.5° with respect to the *z* axis toward the negative *x* semiaxis. Thus, for each position vector we add the projection onto the **a** axis of its component along the **c** axis to its component along the **a** axis of the previous step in order to form the *x*-coordinate in the orthonormal frame. We also project the component along the **c** axis onto the *z* axis to form the *z*-coordinate in the orthonormal frame. The two coordinate frames used are explained in Figure 2.

Table 2. Space Group and Symmetries of α1 iPP (Ref 49)

space group		*C*2/*c*	
symmetries	*X*	*Y*	*Z*
	−*X*	−*Y*	−*Z*
	X	−*Y* + 0.5	*Z* + 0.5
	−*X*	*Y* + 0.5	−*Z* + 0.5

The construction of the hydrogens was performed following ref 51. Equations 1−4 of that reference were used to determine the position vectors of the hydrogens from those of the carbon atoms. Since our chains are isotactic, the coefficients *c* appearing in these equations are the same throughout a chain. A C−H bond length of $l_H = 0.11$ nm and an H−C−H bond angle of $\theta_H = 1.28$ rad were used in the crystal construction.

B. Force Field. For the molecular dynamics computations a fully flexible model was used, which allows the stretching of bonds, bending of bond angles, and twisting of dihedral angles with time.

Our force field follows closely the flexible force field proposed by Logotheti and Theodorou.[52] The origins of this force field lie in the early molecular mechanics work on PP by Theodorou and Suter,[53] which was extended to molecular dynamics by Sylvester, Yip, and Argon.[54] Each PP chain is represented as an assemblage of explicit carbon (C) and pendant hydrogen (H) atoms, while methyl groups (R) are lumped into united atoms. Antoniadis, Samara, and Theodorou[51,55] refined this model and implemented it in connectivity-altering Monte Carlo and MD simulations of atactic, isotactic, and syndiotactic polypropylene. In contrast to the model of Antoniadis et al.,[51] the model of Logotheti and Theodorou[52] was fully flexible (i.e., it did not employ holonomic constraints for the bond lengths).

The minor modifications we introduced here to the PP model of Logotheti and Theodorou[52] were solely intended to facilitate its implementation within the Gromacs[56] computational environment. We did not use a quintic spline for local interactions.

The force field we employed was of the general form

$$\mathscr{V}_{\mathrm{tot}} = \mathscr{V}_{\mathrm{b}} + \mathscr{V}_{\mathrm{a}} + \mathscr{V}_{\mathrm{d}} + \mathscr{V}_{\mathrm{LJ}} \tag{1}$$

The bond stretching potential $\mathscr{V}_{\mathrm{b}}$ consisted of additive distance-dependent contributions from all pairs of bonded atoms, of the form

$$\mathscr{V}_{\mathrm{b}}(r_{ij}) = \frac{1}{2}k_{ij}^{\mathrm{b}}(r_{ij} - b_{ij})^2 \tag{2}$$

with k_{ij}^{b} being the spring constant and b_{ij} the equilibrium bond length for the type of bond considered. Three types of bonds were considered for PP (see Table 3).

The bond angle bending potential $\mathscr{V}_{\mathrm{a}}$ consisted of contributions from all triplets of atoms i, j, k connected by two bonds ij, jk of the form

$$\mathscr{V}_{\mathrm{a}}(\theta_{ijk}) = \frac{1}{2}k_{ijk}^{\theta}(\theta_{ijk} - \theta_{ijk}^{0})^2 \tag{3}$$

with k_{ijk}^{θ} being the bond angle bending spring constant and θ_{ijk}^{0} the equilibrium bond angle. Eight types of bond angles were considered for the finite molar mass and seven for the infinite molar mass iPP systems, the latter lacking R−C−R bond angles which are present at the ends of the former (see Table 3).

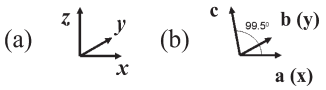

Figure 2. Orthocanonical (a) and monoclinic (b) coordinate frames, with the latter displaying an angle $\beta = 99.5°$ between axes **a** and **c**. The chain axis is parallel to the **c** vector.

A 3-fold intrinsic torsional potential involving four adjacent backbone atoms i, j, k, l was associated with all nonterminal dihedral angles, contributing to the potential term $\mathscr{V}_{\mathrm{d}}$:

$$\mathscr{V}_{\mathrm{d}}(\varphi_{ijkl}) = k_{\varphi}\{1 - \cos[n(\varphi - \varphi_{\mathrm{s}})]\} \tag{4}$$

where $2k_{\varphi}$ is the torsional barrier, $n = 3$ is the multiplicity of the force field (number of local minima) with respect to a dihedral angle (in our case at dihedral angles of −120°, 0°, +120°), and φ_{s} is a constant, which determines at which torsional state the dihedral angle is taken as zero (here φ_{s} is 0°, which corresponds to the trans rotational isomeric state).

Nonbonded interactions (term $\mathscr{V}_{\mathrm{LJ}}$) are active between all pairs of sites (H, C, R) that are more than two bonds apart in the same chain or belong to different chains. These are described by a 12−6 Lennard-Jones potential and, following refs 51 and 52, are distinguished into two categories: local and nonlocal. Local interactions act between sites that are three (1−4 interactions) or four (1−5 interactions) bonds apart along the same chain. Nonlocal interactions act between sites of the same chain that are more than four bonds apart or between sites belonging to different chains. Given the three types of interaction sites, there are six types of local and six types of nonlocal interactions. Each has its own force constants σ_{ij} and ε_{ij} (see Table 4):

$$\mathscr{V}_{ij}^{\mathrm{LJ}}(r_{ij}) = 4\varepsilon_{ij}\left\{\left(\frac{\sigma_{ij}}{r_{ij}}\right)^{12} - \left(\frac{\sigma_{ij}}{r_{ij}}\right)^{6}\right\} \tag{5}$$

Nonlocal Lennard-Jones interactions between all pairs of atoms are modified beyond $r_1 = 1.45\sigma_{\mathrm{R-R}}$ and are brought smoothly to zero[53] at $r_2 = 2.33\sigma_{\mathrm{R-R}}$. r_1 and r_2 were made dependent on $\sigma_{\mathrm{R-R}}$ for all site pairs, unlike previous work,[52] because of a limitation imposed by the simulation package. Since the largest σ_{ij} value was used ($\sigma_{\mathrm{R-R}}$), interactions computed with the current force field differed only little from those computed with the force field of ref 52. In between r_1 and r_2, the potential is brought smoothly to zero

Table 4. Parameter Values of Force Field for the Nonbonded Interactions

interaction type	HH	HC	HR	CC	CR	RR
	local interactions [1−4 (3 bonds), 1−5 (4 bonds)]					
σ_{ij} (nm)	0.2316	0.2762	0.2940	0.3207	0.3386	0.3564
ε_{ij} (kJ/mol)	0.3193	0.3352	0.4305	0.3519	0.4519	0.5808
	nonlocal interactions (> 1−5, intermolecular)					
σ_{ij} (nm)	0.2551	0.3042	0.3195	0.3533	0.3686	0.3838
ε_{ij} (kJ/mol)	0.1849	0.1950	0.2690	0.2054	0.2833	0.3912

Table 3. Parameter Values of Force Field for the Bonded Interactions

bonds		CH			CC			CR	
k_{ij}^{b} (kJ/(mol nm^2))		669888			334944			334944	
b_{ij} (nm)		0.10990			0.14712			0.15065	
bond angles[a]	HCH	HC$_{\mathrm{a}}$C	HC$_{\mathrm{c}}$C	HCR	CC$_{\mathrm{c}}$C	CC$_{\mathrm{a}}$C	CCR	RCR	
k_{ijk}^{θ} (kJ/(mol rad^2))	329.920	398.579	398.579	398.579	604.580	604.580	604.580	604.580	
θ_{ijk}^{0} (deg)	110.099	109.950	108.077	110.271	107.590	111.039	111.526	117.790	
dihedrals		RCCC			CCCC			CCCR	
k_{φ} (kJ/mol)		−			5.86150			−	
φ_s (deg)					0.0				
n					3				

[a] C$_{\mathrm{a}}$ and C$_{\mathrm{c}}$ denote an achiral and a chiral skeletal carbon atom, respectively.

using a fifth-order polynomial (quintic spline,[53] switch function). This function is given by the following equation[53]

$$\mathscr{V}'_{\text{nl-spline}}(r) = \mathscr{V}'^{\text{LJ}}_1(1-\xi)^3\left[1+\left(3+(r_2-r_1)\frac{\mathscr{V}''^{\text{LJ}}_1}{\mathscr{V}'^{\text{LJ}}_1}\right)\xi + \left(6+3(r_2-r_1)\frac{\mathscr{V}''^{\text{LJ}}_1}{\mathscr{V}'^{\text{LJ}}_1}+\frac{(r_2-r_1)^2}{2}\frac{\mathscr{V}'''^{\text{LJ}}_1}{\mathscr{V}'^{\text{LJ}}_1}\right)\xi^2\right] \quad (6)$$

where $\xi = (r - r_1)/(r_2 - r_1)$ and $\mathscr{V}'^{\text{LJ}}_1$, $\mathscr{V}''^{\text{LJ}}_1$, and $\mathscr{V}'''^{\text{LJ}}_1$ stand for the values of the Lennard-Jones pair potential function and its first and second derivatives with respect to distance at $r = r_1$. Because the pair potential is modified beyond r_1, a tail correction should be added to the total potential energy. The tail correction is obtained by integration of the difference between the full Lennard-Jones and the modified potential (eq 6) from r_1 to infinity for all pairs of interaction sites present in the system.[53] In computing tail corrections to the energy and pressure, pair distribution functions were assumed to equal 1 for all site pairs beyond r_1.

To recapitulate, the nonbonded potential of our force field is described by the following equation:

$$\mathscr{V}'_{\text{LJ}} = \mathscr{V}'_{1-4} + \mathscr{V}'_{1-5} + \mathscr{V}'_{\text{nonlocal}} + \mathscr{V}'_{\text{nl-spline}} + \mathscr{V}'_{\text{nl-tails}} \quad (7)$$

The parameters of the flexible force field we employed in eqs 2−5 for the polypropylene chains are given in Tables 3 and 4.

We note that in some simulations some of the crystal chains were held stiff, while in others an additional intramolecular potential encouraging helical conformations was employed, as detailed below.

C. Computational Tools. For our MD simulations we used the open source simulation package GROMACS (Groningen Machine for Chemical Simulations), from version 4.0 onward. Most of the simulations took place with version 4.3. The simulations were carried out on a Beowulf cluster with 98 processors in total made up of 12 nodes, 9 of them consisting of two quad-core Xeon cpus at 2.66 GHz and 16GB RAM (72 processors) and 3 of them consisting of two quad-core Xeon cpus with hyperthreading technology at 2.27 GHz and 8GB RAM (24 processors), coordinated by one master node Xeon dual core CPU at 3 GHz and 4GB ram (two processors).

In the MD simulations, the initial velocities of all atoms were generated from the Maxwell−Boltzmann distribution according to the desired temperature, and the equations of motion were integrated using the Verlet leapfrog algorithm with an integration time step Δt of 1 fs. For the interaction list generation, the grid search method was used every 5 or 10 steps. Energy minimizations were performed with the steepest descent method. MD simulations were carried out in the isothermal−isobaric (NpT), canonical (NVT), and isothermal−isostress ($N\boldsymbol{\sigma}T$) ensembles, as well as in an ensemble where a system cross section is fixed by keeping the periodic continuation vectors along its edges fixed, while the third continuation vector is allowed to fluctuate in length, subject to a fixed normal pressure ($Np_{xx}\mathbf{bc}T$ simulation). To fix the temperature at a prescribed value, the Nosé−Hoover[57] thermostat was used, while pressure and stress were kept constant using a Berendsen[58] barostat and the Parrinello−Rahman[59] method, respectively. The time constants associated with the thermostat and the barostat equaled 0.1 and 1 ps, respectively. A compressibility equal to that of water

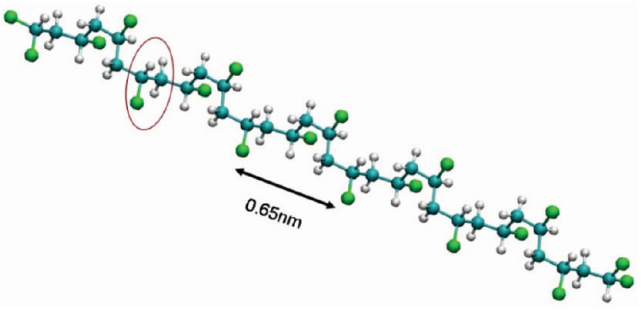

Figure 3. One 3-folded chain of the crystal isolated, showing the step of the helix being $b_{\text{pitch}} = 0.65$ nm. One monomer unit of the chain is encircled. In white are depicted the hydrogen atoms, in light blue the backbone carbon atoms, and in light green the methyl side groups.

(4.5×10^{-5} bar^{-1}) along all directions was used in the Gromacs implementation of the Parrinello−Rahman algorithm. Simulations were performed mostly at 1 bar and at temperatures ranging from 250 to 760 K.

The systems simulated were of various molar masses and sizes. Constituent chains were symmetric, of the type R−(CHR−CH$_2$)$_{x-1}$−CHR$_2$. With the exception of the infinite molar mass crystal (no chain ends), chain lengths were in all cases below the entanglement[60] molar mass (M_e = 7000 g/mol). The system size ranged from 96 (single-phase, independent crystal and melt systems) to 192 chains (sandwich systems). In most calculations, the degree of polymerization was x = 17 (molar mass $42x + 16$ = 730 g/mol), which amounts to $6x - 1$ = 101 interaction sites per chain. The choice of x = 17 was motivated by the availability of experimental measurements of T_m for oligomeric iPP of this length.[61] Clearly, long chains are desirable for simulation predictions to be relevant to commercial iPP. On the other hand, long chains necessitate the use of very large model systems, in order to avoid artifacts associated with the periodic boundary conditions, which can stabilize the crystalline phase. Large model systems require proportionally large computer time to be simulated. A chain length of 17 was found to offer a good compromise between relevance and computational tractability. The total number of sites in the single-phase and sandwich systems was 9696 and 19 392, respectively. The mean edge lengths of the simulated systems at equilibrium at 1 bar and 400 K along the **a**, **b**, and **c** directions were 5.41, 6.36, and 3.97 nm for the pure crystal phase and 11.45, 6.37, and 3.99 nm for the sandwich, respectively. These system sizes were computationally tractable and at the same time yielded predictions that were free of system size effects. Trial runs with a sandwich system doubled in size gave practically the same melting temperature. Each MD simulation took from some minutes to a couple of days real time.

D. Construction of Crystalline Configurations of Finite Molar Mass. Crystalline configurations of finite molar mass were derived from the infinite molar mass α1 crystal discussed in section III.A by excising −(CHR)− sections from specific positions along the infinite chains and converting the skeletal carbons to which these sections used to be connected into terminal R groups. First we decide how many unit cells the model system will encompass in the x and y directions. This determines the number of chains going through each xy cross section of the model system. For our 17mer−96 chain system (Figure 1), the number of unit cells was chosen as 8 and 3 along the x and y axes, respectively. As discussed in connection with Figure 2, the x and y axes are directed along the **a** and **b** crystallographic axes, respectively. The length of

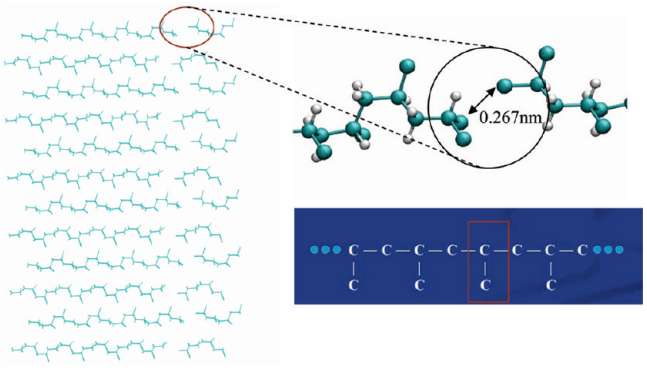

Figure 4. Part of the infinite molar mass α1 crystal, which was excised so as to create the finite 17mer crystal system. The sites indicated by the arrows were converted from carbons to united-atom methyl groups.

the monoclinic simulation cell along the **c** direction, which is inclined by 9.5° with respect to the *z* axis of an orthonormal frame of reference, controls the degree of polymerization of the chains. To obtain a 17mer crystalline model system (Figure 3), we constructed 6 unit cells along this axis, added the hydrogens as described in section III.A, and then removed a −(CHR)− group from each of the 96 chains present, thus forming a lamella of finite thickness along the **c**-direction, characterized by periodic boundary conditions along **a**, **b**, and **c**. As mentioned above, all carbons flanking the excised groups were converted to methyls, such that the finite chains all terminated in $-CHR_2$ groups (see Figure 4). Following the excision and chemical mutation of terminal atoms, the configuration was subjected to energy minimization and then to Parrinello−Rahman MD at 1 bar and 250 K for 2 ns. Thus, the finite molar mass crystal was allowed to equilibrate subject to the force field described in section III.B. After this equilibration, the closest distance between R groups belonging to different lamellae increased from its initial value of 0.267 nm (Figure 4) to 0.350 ± 0.08 nm.

E. Generation of Sandwich Model Systems. A very important role in our investigations of solid−liquid equilibrium is played by our sandwich configurations, in which solid and liquid subdomains are brought into molecular contact. What we call a sandwich system is essentially a set of alternating slabs of crystalline and amorphous material, characterized by periodic boundary conditions in all three directions. Extreme care was taken in order to ensure that the two subsystems comprising the sandwich are equilibrated and free of defects.

Sandwich model systems were characterized by monoclinic periodic boundary conditions identical to those of the α1 crystal. Two types of sandwich model systems were studied: one in which the solid/liquid interface was parallel to the **bc** crystallographic plane, with the lateral surfaces of helical chains at the edges of the crystalline domain exposed to the melt; and a second one, in which the solid/liquid interface was parallel to the **ab** crystallographic plane, with the ends of chains of the crystalline domain being exposed to the melt. Only results from the first type of sandwich system will be discussed here. The second type of sandwich, wherein the ends of crystalline chains were exposed to the melt, was found less prone to crystallize and therefore left for future study.

For the creation of a sandwich system we adopted the following procedure:

First, we created a lamellar crystal with a primary simulation box containing 96 17mer chains, as described in section III.D. The crystal was equilibrated via energy minimization, keeping its edge lengths constant along **a**, **b**, and **c**. After equilibration, the lamella of crystalline chains was separated from its periodic images along the **a** crystallographic direction, creating a crystalline subdomain that was finite along the **a** direction and periodically continuous along the **b** and **c** directions, with free surfaces parallel to the **bc** plane.

Next, an amorphous (melt) phase was generated within a monoclinic simulation box characterized by three-dimensional periodic boundary conditions, whose edge vectors along the **b** and **c** directions were identical to those of the crystal subdomain with which it would be paired. The simulation box of the amorphous phase contained an equal number (96) of 17mer iPP chains as the crystalline subdomain. It was generated by melting a crystalline system of the type described in section III.D and then equilibrating it via a ∼15 ns long $N\boldsymbol{\sigma}T$ MD simulation, during which the edge vectors of the simulation box fluctuated. This simulation of the melt phase was of value in its own right in our strategy for determining T_m (see section III.F). It also served as a starting point for generating the liquid subdomain of a sandwich system, as follows. The final configuration from the melt $N\boldsymbol{\sigma}T$ MD simulation was subjected to energy minimization. Subsequently, the periodic continuation vectors of the amorphous simulation box along **b** and **c** were modified in small steps, with each modification being followed by an energy minimization of the amorphous system, until **b** and **c** became identical to those of the α1 crystal. Vector **a** was also adjusted in these successive minimizations, to ensure that the amorphous configuration always retained the same density as the initial one, which was equilibrated with $N\boldsymbol{\sigma}T$ MD. After imposition of the crystal **b** and **c** vectors on the amorphous phase, as described above, the primary amorphous box was separated from its periodic images along the **a** direction, giving rise to a slab of amorphous polymer that was periodically continuous along the **b** and **c** directions, but finite along the **a** direction. The slab consisted exclusively of entire chains; if a chain started within the primary simulation box, it was included in the slab in its entirety, i.e., without being truncated and periodically continued across the faces parallel to the **bc** plane. As a result, while the slab density was close to the experimental melt density in its middle region, the regions close to its two surfaces were sparse, consisting largely of tentacles of chains protruding into vacuum. Subjecting this slab of finite thickness to energy minimization brought about considerable retraction of the tentacles and densification of the surface regions. This energy-minimized slab served as our initial configuration for the liquid polymer subdomain of the sandwich.

The energy-minimized crystalline and amorphous subdomains were brought next to each other, such that their edge vectors along the **b** and **c** directions coincided and their edge vectors along the **a** (x) direction fell on the same line. Periodic conditions along all three directions were imposed on the composite system. The two subdomains were placed at some distance from each other along the x axis to avoid excluded volume overlaps between crystalline and amorphous chains (see Figure 5a,b). Clearly, the gaps present between the subdomains at this stage have to be closed and the two phases have to be brought into molecular contact. To accomplish this, an $Np_{xx}\mathbf{bc}T$ simulation of the composite system under three-dimensional periodic boundary conditions was undertaken, during which crystal atoms were prevented from moving along the **b** and **c** direction by applying constraints, while being able to move freely in the **a** direction. After 2 ns of simulation, both gaps between the crystalline and amorphous regions were closed and well-equilibrated interfaces characterized by stable total energy,

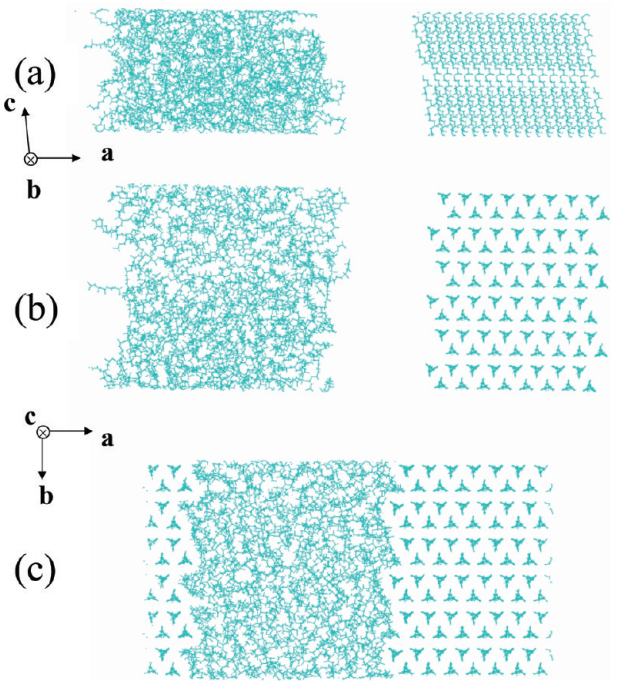

Figure 5. Sandwich system (a) viewed along the *y* direction just after the energy minimization process. Crystal and melt subsystems are far apart. (b) The same system viewed along the **c** axis of the monoclinic simulation box (i.e., the axis of the chains in the crystalline domain) (c) Final sandwich system viewed along the **c** axis; here, crystal and melt subsystems have been brought in molecular contact.

density, and pressure tensor profiles were formed on both sides of the crystalline (or amorphous) subdomain (see Figure 5c). These equilibrated sandwich structures were employed as initial configurations in the MD simulations described below. We note that a melt domain size of 96 chains proved sufficient for bulk conditions to prevail in the middle region of the melt slabs at equilibrium, as evidenced by a flat density profile at a value indistinguishable from that of the bulk melt and a flat, isotropic pressure tensor profile in this region.

F. Solid−Liquid Equilibrium in the Presence of a Constraining Potential. Gibbs−Duhem Integration. The rate of homogeneous nucleation is extremely slow in polymers. Experimentally,[62−64] undercoolings on the order of 100 K are necessary for the emergence of critical nuclei that can lead to freezing, and molecular simulation can address nucleation only by invoking techniques for the analysis of infrequent events. On the other hand, heating a crystal at rates accessible by MD is likely to lead[13,19,38] to significant overheating (hysteresis of melting). Given these problems, which are much more severe in iPP than in polyethylene, the strategy adopted in this work is to compute solid−liquid equilibrium by analyzing the phenomenon of crystal growth onto an already existing crystal facet and of melting of that facet. Starting from a biphasic sandwich structure, generated as described in section III.E, and simulating it at 1 bar under a variety of temperatures, we intend to determine the temperature below which the solid phase grows at the expense of the melt phase and above which the melt phase grows at the expense of the crystal phase. This temperature will be our computational estimate of the thermodynamic T_m. This strategy has been employed successfully in the case of simple liquids,[65−67] water,[68] and *n*-octane.[8]

Even this strategy is not straightforward to implement for iPP. Experimentally, the crystal growth rate for high-molar-mass iPP has been reported[69−71] as 2.2×10^{-7} m/s. This means that, in order to observe growth of a facet by an average distance of 1 Å, one would need to simulate for 450 μs, which is prohibitively long for MD simulations on the computers available today. This leads us to study an oligomeric analogue (in our case, a 17mer), in which molecular mobility should be by several orders of magnitude higher than in the entangled high-molar-mass melt, leading to a much larger growth rate. In the case of iPP, however, a problem arises with resorting to an oligomeric analogue. For a short chain melt the equilibrium melting point T_m is lower, coming closer to the glass temperature[72,73] T_g. (For iPP, $T_g \cong 265$ K, exhibiting a weaker dependence on molar mass than T_m.) Segmental dynamics in the cooled oligomer slows down precipitously due to the proximity to the glass transition, narrowing the temperature window over which crystal growth can be observed by MD simulation. In practice, no appreciable growth of the crystal subdomain is observed over MD runs of hundreds of nanoseconds at any temperature between 250 and 480 K. This leads us to the idea of introducing a constraining potential encouraging the chains to register onto the crystal facet. This constraining potential will, of course, modify the melting point. If we manage, however, to estimate the melting point reliably for some value of the constraining potential and have a means for extrapolating that estimate down to zero constraining potential, we will have a reliable estimate of T_m from simulation.

The constraining potential we devised in this work is a harmonic potential between all pairs of skeletal carbons separated by six bonds along a chain, which keeps their distance close to the value $b_{pitch} = 0.65$ nm it adopts in the 3_1 helix of iPP. We will call this potential $\lambda \mathcal{V}_{constr}(\mathbf{r})$, with $\mathbf{r}$ being the vector of Cartesian coordinates of all sites in our model system. In our case

$$\lambda \mathcal{V}_{constr}(\mathbf{r}) = \lambda \sum_{i_{ch}=1}^{N} \sum_{i=1}^{2x-7} \left\{ \frac{1}{2} k_{CC}^{b} (|\mathbf{r}_{C_{i+6},i_{ch}} - \mathbf{r}_{C_i,i_{ch}}| - b_{pitch})^2 \right\} \quad (8)$$

where $N = 192$ is the total number of chains in the sandwich system, $x = 17$ is the degree of polymerization, the total number of skeletal carbons per chain being $2x - 1$, and $\mathbf{r}_{C_{i,ich}}$ stands for the position vector of the *i*th skeletal carbon of the i_{ch}th chain (compare helical conformation of Figure 3). The spring constant k_{CC}^{b} is equal to that used for stretching of carbon−carbon bonds, listed in Table 3. The coefficient λ is a coupling parameter used to scale the magnitude of the constraining potential; it will be varied from values around 1 (strong bias toward helical conformations) down to 0 (unconstrained iPP) in our simulations and plays a significant role in our analysis.

Assuming that we have determined the equilibrium melting point, T_m, for a certain value of λ, how do we expect T_m to change, if we change λ? The derivative $(\partial T_m/\partial\lambda)|_p = (\partial T_m/\partial\lambda)|_{p,eq}$ can be estimated through a straightforward thermodynamic argument that is reminiscent of the Gibbs−Duhem integration scheme proposed by Kofke.[74,75] Instead of modulating pressure, as in the Clapeyron equation invoked by the original Gibbs−Duhem integration, here we will modulate the parameter λ entering the Hamiltonian of the system, under isobaric conditions. To our knowledge, this idea of capturing solid−liquid equilibrium by simulation via continuous modulation of a parameter entering the system Hamiltonian has not been proposed before.

In the presence of the constraining potential, the potential energy function of the system becomes

$$\mathscr{V}_{\mathrm{mod}}(\mathbf{r};\lambda) = \mathscr{V}_{\mathrm{tot}}(\mathbf{r}) + \lambda \mathscr{V}_{\mathrm{constr}}(\mathbf{r}) \tag{9}$$

where $\mathscr{V}_{\mathrm{tot}}(\mathbf{r})$ is the total potential energy of unconstrained iPP, given by eq 1.

Consequently, the Hamiltonian of the constrained system is

$$\mathscr{H}(\mathbf{r},\mathbf{p};\lambda) = \mathscr{K}(\mathbf{p}) + \mathscr{V}_{\mathrm{tot}}(\mathbf{r}) + \lambda \mathscr{V}_{\mathrm{constr}}(\mathbf{r}) \tag{10}$$

with $\mathscr{K}(\mathbf{p})$ being the kinetic energy as a function of the momenta of the sites.

Thermodynamic properties within single-phase regions can be derived from the fundamental equation in the Gibbs energy representation, where the Gibbs energy G is related to the isothermal−isobaric partition function Q_{NpT} as

$$G(N,p,T;\lambda) = -k_{\mathrm{B}}T \ln Q_{NpT\lambda} \tag{11}$$

with

$$Q_{NpT\lambda} = \frac{1}{V_0}\int \mathrm{d}\mathbf{r}\,\mathrm{d}\mathbf{p} \exp[-\beta\mathscr{H}(\mathbf{r},\mathbf{p};\lambda)] \exp(-\beta pV)\,\mathrm{d}V \tag{12}$$

and $\beta = 1/(k_{\mathrm{B}}T)$. V_0 is an arbitrary volume[76] that nondimensionalizes Q_{NpT}. It is the same between liquid- and solid-phase partition functions. More rigorously, a formulation expressing G in terms of the stress tensor, as an integral over the strain tensor, would be appropriate for the solid phase, but we retain the formulation in terms of a single scalar pressure p for simplicity and transparency.

From eq 11, the derivative of the single-phase Gibbs energy with respect to any parameter λ entering the Hamiltonian is

$$\left.\frac{\partial G}{\partial \lambda}\right|_{N,p,T} = -k_{\mathrm{B}}T \frac{1}{Q_{NpT\lambda}} \frac{\partial Q_{NpT\lambda}}{\partial \lambda} \tag{13}$$

Furthermore, from eq 12

$$\begin{aligned}\frac{1}{Q_{NpT\lambda}} \frac{\partial Q_{NpT\lambda}}{\partial \lambda} &= \frac{\frac{1}{V_0}\int \mathrm{d}\mathbf{r}\,\mathrm{d}\mathbf{p}\,\mathrm{d}V\left[-\beta\frac{\partial \mathscr{H}}{\partial \lambda}\right] \exp(-\beta\mathscr{H}(\mathbf{p},\mathbf{r};\lambda)) \exp(-\beta pV)}{\frac{1}{V_0}\int \mathrm{d}\mathbf{r}\,\mathrm{d}\mathbf{p}\,\mathrm{d}V \exp(-\beta\mathscr{H}(\mathbf{p},\mathbf{r};\lambda)) \exp(-\beta pV)} \\ &= \left\langle -\beta\frac{\partial \mathscr{H}}{\partial \lambda}\right\rangle_{NPT\lambda}\end{aligned} \tag{14}$$

For our case (eq 10), eqs 13 and 14 yield

$$\left.\frac{\partial G}{\partial \lambda}\right|_{N,p,T} = \langle \mathscr{V}_{\mathrm{constr}}(\mathbf{r})\rangle_{NpT\lambda} \tag{15}$$

If, at some value of λ, phase equilibrium has been established between liquid (l) and solid (s) phases, the chemical potential or, equivalently, the Gibbs energy per molecule, will be the same between the two phases, each consisting of N (=96) molecules:

$$\begin{aligned}&\mu_{\mathrm{l}}(p,T,\lambda) = \mu_{\mathrm{s}}(p,T,\lambda),\\ \text{or } &\frac{G_{\mathrm{l}}(N,p,T,\lambda)}{N} = \frac{G_{\mathrm{s}}(N,p,T,\lambda)}{N},\\ \text{or } &G_{\mathrm{l}}(N,p,T,\lambda) - G_{\mathrm{s}}(N,p,T,\lambda) = 0\end{aligned} \tag{16}$$

If we change the parameter λ by a small amount $\mathrm{d}\lambda$ and maintain the phase equilibrium under isobaric conditions, eq 16 will continue to hold. The equilibrium coexistence temperature will shift by $\mathrm{d}T$, such that

$$\begin{aligned}&\left\{\frac{\partial}{\partial \lambda}[G_{\mathrm{l}}(N,p,T,\lambda) - G_{\mathrm{s}}(N,p,T,\lambda)]\right\}_{N,p,T} \mathrm{d}\lambda|_{N,p,\mathrm{eq}}\\ &+\left\{\frac{\partial}{\partial T}[G_{\mathrm{l}}(N,p,T,\lambda) - G_{\mathrm{s}}(N,p,T,\lambda)]\right\}_{N,p,\lambda} \mathrm{d}T|_{N,p,\mathrm{eq}} = 0\end{aligned}$$

hence

$$\left.\frac{\partial T}{\partial \lambda}\right|_{p,\mathrm{eq}} = -\frac{\left\{\frac{\partial}{\partial \lambda}[G_{\mathrm{l}}(N,p,T,\lambda) - G_{\mathrm{s}}(N,p,T,\lambda)]\right\}_{N,p,T}}{\left\{\frac{\partial}{\partial T}[G_{\mathrm{l}}(N,p,T,\lambda) - G_{\mathrm{s}}(N,p,T,\lambda)]\right\}_{N,p,\lambda}} \tag{17}$$

where the subscript N has been dropped from the left-hand side, recognizing that both T and λ are intensive properties of the system. Now, from eq 15

$$\begin{aligned}&\left\{\frac{\partial}{\partial \lambda}[G_{\mathrm{l}}(N,p,T,\lambda) - G_{\mathrm{s}}(N,p,T,\lambda)]\right\}_{N,p,T}\\ &\quad = \langle \mathscr{V}^{\mathrm{l}}_{\mathrm{constr}}(\mathbf{r})\rangle_{NpT\lambda} - \langle \mathscr{V}^{\mathrm{s}}_{\mathrm{constr}}(\mathbf{r})\rangle_{NpT\lambda}\end{aligned} \tag{18}$$

while

$$\begin{aligned}&\left\{\frac{\partial}{\partial T}[G_{\mathrm{l}}(N,p,T,\lambda) - G_{\mathrm{s}}(N,p,T,\lambda)]\right\}_{N,p,\lambda}\\ &= -S_{\mathrm{l}}(N,p,T,\lambda) + S_{\mathrm{s}}(N,p,T,\lambda)\\ &= \frac{1}{T}[-H_{\mathrm{l}}(N,p,T,\lambda) + H_{\mathrm{s}}(N,p,T,\lambda)] + \frac{1}{T}[G_{\mathrm{l}}(N,p,T,\lambda)\\ &\qquad - G_{\mathrm{s}}(N,p,T,\lambda)]\end{aligned} \tag{19}$$

with S and H being the entropy and enthalpy, respectively.

At equilibrium, the last term on the right-hand side of eq 19 is 0, by eq 16. Furthermore, from the partition function of eq 12 applied separately to the solid and liquid phases, the difference in enthalpies can be computed as

$$\begin{aligned}&-H_{\mathrm{l}}(N,p,T,\lambda) + H_{\mathrm{s}}(N,p,T,\lambda)\\ &\quad = -\langle \mathscr{V}^{\mathrm{l}}_{\mathrm{mod}} + pV^{\mathrm{l}}\rangle_{NpT\lambda} + \langle \mathscr{V}^{\mathrm{s}}_{\mathrm{mod}} + pV^{\mathrm{s}}\rangle_{NpT\lambda}\end{aligned} \tag{20}$$

given that the mean kinetic energy is the same in both phases.

From eqs 17−20, taking into account eq 16, we finally obtain

$$\begin{aligned}\left.\frac{\partial T}{\partial \lambda}\right|_{p,\mathrm{eq}} = T\{&[\langle \mathscr{V}^{\mathrm{l}}_{\mathrm{constr}}\rangle_{NpT\lambda} - \langle \mathscr{V}^{\mathrm{s}}_{\mathrm{constr}}\rangle_{NpT\lambda}]/[\langle \mathscr{V}^{\mathrm{l}}_{\mathrm{tot}}\rangle_{NpT\lambda}\\ &- \langle \mathscr{V}^{\mathrm{s}}_{\mathrm{tot}}\rangle_{NpT\lambda} + \lambda[\langle \mathscr{V}^{\mathrm{l}}_{\mathrm{constr}}\rangle_{NpT\lambda} - \langle \mathscr{V}^{\mathrm{s}}_{\mathrm{constr}}\rangle_{NpT\lambda}]\\ &+ p[\langle V^{\mathrm{l}}\rangle_{NpT\lambda} - \langle V^{\mathrm{s}}\rangle_{NpT\lambda}]]\}\end{aligned} \tag{21}$$

Equation 21 can be used to predict how the melting temperature will shift upon changing the coupling parameter λ. For this, two equilibrium single-phase simulations at N, p, T, and λ are needed. The liquid-phase simulation will yield

$\langle \mathcal{V}^{l}_{constr} \rangle_{NpT\lambda}$, $\langle \mathcal{V}^{l}_{tot} \rangle_{NpT\lambda}$, and $\langle V^{l} \rangle_{NpT\lambda}$, while the solid-phase simulation will yield $\langle \mathcal{V}^{s}_{constr} \rangle_{NpT\lambda}$, $\langle \mathcal{V}^{s}_{tot} \rangle_{NpT\lambda}$, and $\langle V^{s} \rangle_{NpT\lambda}$ as equilibrium ensemble averages.

Our computational strategy for obtaining T_m employs three series of NpT MD simulations at progressively lower λ, therefore of T: one for a pure (periodically continuous in three dimensions) solid phase, one for a pure liquid phase, and one for a sandwich system of solid and liquid phases at coexistence. All simulations are carried out at $p = 1$ bar, with initial configurations generated as described in sections III.D and E. The strategy proceeds as follows:

1. Starting with $\lambda = \lambda_{max}$, simulate the sandwich system under a variety of temperatures to pinpoint the equilibrium temperature $T_m(\lambda = \lambda_{max})$, at which none of the subdomains of the sandwich grows at the expense of the other. An equilibrium temperature can be defined readily for this strong constraining field, but it is, of course, too high in relation to the actual melting temperature of the oligomer.

2. Simulate a pure crystal phase and a pure liquid phase at the current value of λ and at the equilibrium temperature $T_m(\lambda)$ determined for it by use of the sandwich. Both single-phase simulations should be stable, if the sandwich simulations have been executed correctly. From these two simulations, obtain $\langle \mathcal{V}^{l}_{constr} \rangle_{NpT\lambda}$, $\langle \mathcal{V}^{l}_{tot} \rangle_{NpT\lambda}$, $\langle V^{l} \rangle_{NpT\lambda}$ and $\langle \mathcal{V}^{s}_{constr} \rangle_{NpT\lambda}$, $\langle \mathcal{V}^{s}_{tot} \rangle_{NpT\lambda}$, $\langle V^{s} \rangle_{NpT\lambda}$ as ensemble averages.

3. Change the coupling parameter λ by a small amount $\Delta\lambda < 0$. Using eq 21, estimate the expected change ΔT_m in melting point expected as a result of changing λ, hence the equilibrium temperature T_m corresponding to the new value of λ.

4. Conduct a sandwich simulation at the new value of λ and at the estimated value of the equilibrium temperature. If one of the subdomains of the sandwich exhibits a tendency to increase at the expense of the other, adjust the temperature accordingly to achieve equilibrium.

5. Return to step 2.

In this way, an equilibrium curve is traced on the $T-\lambda$ plane. Continuation of this curve down to $\lambda = 0$ yields the equilibrium melting point of our polymer model. We emphasize that small steps in λ must be taken, as eq 21 presupposes equilibrium between the two phases. Step 4 above has been designed precisely in order to correct errors in T_m introduced by the approximation of the derivative in eq 21 by a ratio of finite differences.

IV. Results and Discussion

A. Force Field Validation and Properties of the Finite Molar Mass Crystal. Our first priority before studying the crystallization process was to verify that the force field was capable of representing the α1 monoclinic crystal structure of iPP. Starting from the crystallographic data for the α1 phase, we constructed a crystalline model configuration of infinite molar mass chains without ends as outlined in section III.A. The primary simulation box consisted of 8, 3, and 6 unit cells along the **a**, **b**, and **c** crystallographic directions. The total potential energy $\mathcal{V}_{tot}(\mathbf{r})$ of the model system (eq 1) was minimized with respect to all site coordinates **r** in the primary box at constant box edge lengths, using the steepest descent method. Energy minimization brought about a small adjustment of atomic coordinates, the root-mean-squared deviation between crystallographic and energy-mimimized configurations being 0.243 Å. Next, 2 + 20 + 2 + 20 + 20 ns long MD simulations of the model system were conducted with the Parrinello−Rahman method in the range of temperatures of 250−550 K, keeping the system for 2 ns at each of the temperature levels of 250 and 350 K, and heating it in 100 K intervals, each time for 20 ns. This range encompasses the theoretical[17] (∼456 K) and experimental[73] (∼438 K) melting point of iPP crystals. The orientational order of helical chains in the system was preserved, and the lattice parameters stayed close to their crystallographic values. Even at the highest temperatures simulated, the crystal did not collapse into a liquid phase. Apparently, periodic boundary conditions in the infinite chain model system were too confining to allow melting to occur at the heating rate employed (compare against behavior of oligomeric model system discussed in section IV.B). A comparison between lattice parameters obtained with our force field at 250 K and experimental crystallographic values is given in Table 5. The final configuration of the aforementioned MD run at 250 K was subjected anew to energy minimization, to check whether atoms would return to their initial positions at the minimum. This did happen to an excellent approximation. These tests convinced us that the simple force field described in section III.A, developed for the description of amorphous and glassy states of iPP,[52] performs quite well in the crystalline state as well.

Table 5. Crystal Structure of 17mer System at 250 K

unit cell constants	a (nm)	b (nm)	c (nm)	β (deg)
experiment[a]	0.663	2.078	0.650	99.5
simulation	0.664 ± 0.001	2.093 ± 0.001	0.655 ± 0.001	99.6

[a] a, b, and c are the lattice parameters, and β is the angle between **c** and **a** axes in the monoclinic α1 crystal.

B. Melting of the Oligomer Crystal. A crystalline configuration of 17mer chains in the α1 phase, with the primary box containing 96 chains, was prepared from the crystallographic structure of the infinite molar mass crystal as described in section III.D. The energy of this configuration was minimized with respect to atomic coordinates and with respect to the length of the **c** axis, allowing different images of the periodic lamella of helical macromolecules to adjust their distance from each other. Energy minimization was performed using the steepest descent method, with a maximum force convergence criterion of 10 kJ/(mol nm) and initial step size of 0.01 nm for atomic coordinates. In less than 1000 steps the minimization converged, showing that the lamellar configuration created by cutting the infinite chains is close to a crystalline minimum of the system. The lamellar period along the **c** direction at the minimum was found equal to 3.93 nm. Next, the energy minimized α1 configuration of oligomeric chains was used as initial configuration for a 2 ns NpT MD simulation using the Nosé−Hoover thermostat coupling[57] and the isotropic Parrinello−Rahman pressure coupling.[59] An isotropic pressure of 1 bar and a temperature of 250 K were used in this simulation. The crystal structure remained stable. The final configuration from this simulation was used as input to an isobaric ($p = 1$ bar) heating run using the "annealing" option of Gromacs. Temperature was increased from 250 to 350 K at a rate of 5 K/ns. At 350 K the system was simulated further in the NpT ensemble for another 2 ns. Constancy of the total energy and its components, as well as of the density, indicated that the system had reached equilibrium in the solid state at 350 K. The system was heated further from 350 to 450 K at a rate of 5 K/ns under a pressure of 1 bar. For this stage of the heating run we used the Berendsen anisotropic pressure coupling,[58] which can better deal with quick oscillations in box dimensions that are expected in the vicinity of the solid to liquid transition, following the suggestions of the simulation package developers. No first-order transition was observed in this range of temperatures. Finally, the heating was continued at the same

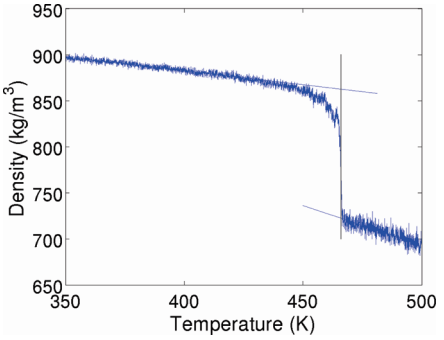

Figure 6. First-order melting transition, as detected by monitoring the density during isobaric heating of the crystal of 17mer chains from 350 to 500 K. The simulation box contained 96 chains. The transition took place around 466 K, close to the experimental melting point of real iPP crystals. The thin straight lines were used to estimate the thermal expansion coefficients in the solid and liquid states and the change in density upon melting.

rate from 450 to 550 K. A discontinuous change in the density and in the potential energy was observed at around 466 K, as seen characteristically in Figures 6 and 7, respectively. An amorphous melt was the product of the first-order phase transition. Its conformational, packing, thermodynamic, and dynamical properties were found to be practically identical to those reported in our previous simulations of molten iPP in the same temperature range.[52]

The temperature at which melting is observed in our isobaric heating simulations is by ~10 K higher than the equilibrium melting temperature estimated experimentally[17] for pure crystalline high-molar mass iPP. It is, however, by roughly 120 K higher than[61] the equilibrium melting point of 17mer iPP. This significant overheating is caused by the high heating rate employed in our simulations. Similar overheating effects have been reported before in connection with melting simulations of simpler molecules, as discussed above.[13,19,38] A more reliable estimate of the equilibrium T_m for our 17mer is obtained through the new computational scheme we outlined in section III.F. Results from that scheme are presented below in sections IV.C and IV.D.

Despite our overestimation of the melting temperature, it is useful to extract some key thermodynamic properties characteristic of the crystal and melt states and of the phase transition between them from our isobaric heating simulations.

From Figure 6, the thermal expansion coefficient in the crystal (350−450 K) is found to be 3.40×10^{-4} K^{-1}, while the experimental[77] one is 3.45×10^{-4} K^{-1}. The thermal expansion coefficient in the melt is 10.1×10^{-4} K^{-1}, while the experimental[78] one is 8.0×10^{-4} K^{-1}. The change in density upon melting from the results plotted in Figure 6 is $\Delta_{fus}\rho = \rho_l - \rho_s = -140$ kg/m^3, while the experimental $\Delta_{fus}\rho$, considering the density of the crystal at 300 K, the thermal expansion coefficient of the crystal, and the density of the melt phase at 459 K, is estimated as −139 kg/m^3. The heat of fusion $\Delta_{fus}H = H_l - H_s$ from Figure 7 is estimated as 135 kJ/kg, while the experimental[79] one for a semicrystalline material is reported as 110 kJ/kg and for pure crystal[80] as 138 kJ/kg. The heat capacity in the crystal and melt states, from the low- and high-temperature slopes of the lower part of Figure 7, is 3.57 and 3.91 kJ/(kg K), respectively, with the corresponding experimental[81] values being 2.42 and 2.73 kJ/(kg K), respectively. The Δc_p between the melt and crystal state from simulation is found to be 0.34 kJ/(kg K), while from experiment it is 0.31 kJ/(kg K). Note that heat capacity values are not expected to be accurately determined from our

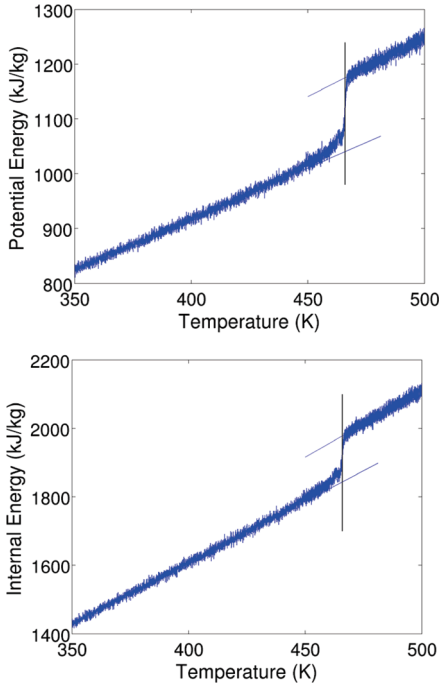

Figure 7. First-order melting transition, as detected by monitoring the potential energy and the internal energy (sum of potential and kinetic energies) during isobaric heating of the crystal of 17mer chains from 350 to 500 K. The thin straight lines were used to estimate the heat capacities in the solid and liquid states from the bottom plot and the heat of fusion from both plots.

MD simulations, which treat vibrations classically with a united-atom representation of methyl groups and a simplified bonded potential. Nevertheless, the difference Δc_p in heat capacity between liquid and solid is estimated quite reasonably by our simulations. In the solid phase, our classical simulation should yield the Dulong−Petit value of $3R$ per Avogadro's number of interaction sites present. Indeed, our simulation estimate of the heat capacity from the slope of the enthalpy−temperature curve in the crystal is 245.6 kJ/(K mol simulation boxes). Our simulation estimate from fluctuations in the instantaneous enthalpy[76] is 250.8 kJ/(K mol simulation boxes) at 250 K and 247.4 kJ/(K mol simulation boxes) at 350 K. These simulation estimates should be compared to the theoretical (Dulong−Petit) one of $[3(101 \times 96) - 6]R = 241.8$ kJ/(K mol simulation boxes); the simulation box contained 96 chains, each consisting of 101 interaction sites, and six degrees of freedom must be subtracted because the energy is invariant to overall translation and rotation of the box. The constancy of the internal energy (potential energy plus kinetic energy) of the crystal during our simulations at 250 and 350 K and the conformity of our crystal simulations to the Dulong−Petit law are displayed in Figure 8. Note that the pV contribution to enthalpy was negligible, in comparison to the internal energy, under the conditions examined here.

C. Crystallization in the Presence of a Constraining Potential. The first attempt we made to crystallize the system was to reverse the isobaric heating MD process described above. Using liquid configurations obtained from melting at 470−480 K as initial configurations, we conducted MD simulations of duration 20 to 100 ns at a variety of temperatures between 480 and 250 K. No appreciable ordering was found to occur in any of these simulations. At the high end of this temperature range the melt chains were quite mobile but exhibited no propensity to adopt helical conformations and

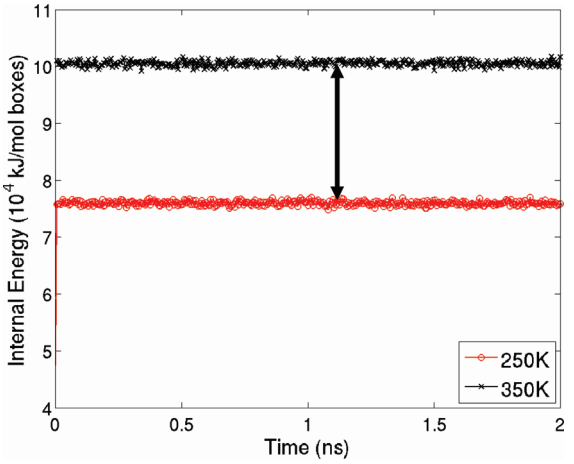

Figure 8. Internal energy of the crystal structure per mol of simulation boxes, evaluated as the sum of potential and kinetic energies, at 250 and 350 K. The double-headed arrow shows the theoretical value for the difference in internal energy expected between the two temperatures based on the Dulong−Petit law, 241.8 ΔT kJ/(mol boxes), with T in K (please see text for details).

pack into a crystalline phase. On the other hand, at the low end of this temperature range, which encompasses T_g, molecular motion became very sluggish. The center-of-mass diffusivity of chains dropped precipitously, as expected from Vogel−Fulcher or WLF-type equations.[52] Short helical sequences were observed to form in isolated chains but were unable to propagate through the melt. The effort to crystallize by isobaric cooling of the melt was therefore abandoned, concluding that, even for 17mer iPP, the nucleation rate of the crystalline phase from the melt is too low for nucleation to be observed by "brute force" MD.

Next, sandwich model structures were formed as described in section III.D, each structure consisting of 192 17mer chains divided equally between the crystalline and melt subdomains. 20−40 ns long NpT MD simulations of the sandwich structures were undertaken at a variety of temperatures, to see whether melt chains would crystallize onto the crystalline faces of the lamella in the sandwich at low temperatures. Again, no appreciable signs of spontaneous crystal growth were observed. At low temperature, the lamellar faces did act as a template inducing weak orientation in the nearby melt chains, but this ordering was unable to propagate through the system because of the sluggish segmental dynamics. We concluded that crystal growth in 17mer iPP is too slow to be captured by "brute force" MD simulation, at least based on the force field we employed.

In order to overcome the difficulties described above, we decided to help the crystallization process by introducing a constraining potential that encourages helical conformations in the polymer. The potential of eq 8 was developed, and sandwich simulations with the modified force field of eq 9 were undertaken. This potential is, of course, compatible with the conformations adopted in the crystalline state, which it is designed to mimic. It causes the chains to become much stiffer, however, and brings about significant changes in the conformational distribution of the melt. To prevent the MD simulation from becoming unstable, the constraining potential was introduced gradually. First, an energy-minimized, compacted sandwich system was simulated at 350 K and 1 bar for 20 ns in the Np_{xx}**bc**T ensemble in the absence of any constraining potential, using anisotropic pressure coupling. In all simulations described in the following, the Nosé−Hoover[57] thermostat was used. In this initial

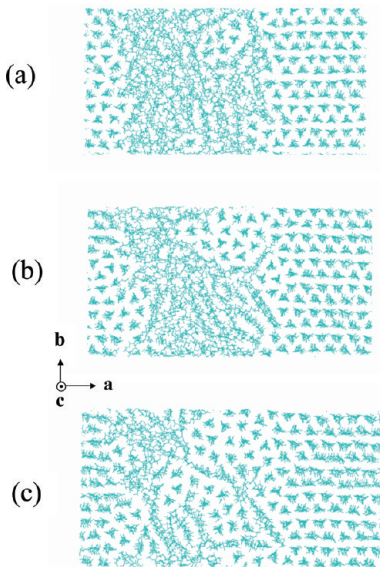

Figure 9. Crystallization of sandwich system during the last 20 ns of simulation at 520 K subject to a constraining potential with $\lambda = 0.3$ in the melt and $\lambda = 1.194$ in the crystalline subdomains, as stated in the text. Here are shown configurations after (a) 3 ns, (b) 7 ns, and (c) 9 ns of simulation.

simulation, the dimensions of the sandwich along the **b** and **c** directions were kept fixed, as the crystal atoms were prevented from moving in these directions. Next, the temperature of the sandwich system was raised to 400 K, while starting to impose the constraining potential on the melt subsystem with $\lambda = 1/30$. MD simulation at this λ value was conducted for 7 ns, after which λ was raised to 0.10 and the simulation continued for 8 ns. 14 ns of simulation at a value of $\lambda = 0.3$ imposed on the melt followed, still at 400 K. Next, the temperature was raised to 440 K, still at $\lambda = 0.3$, and the sandwich system was simulated for another 10.7 ns. At this point, the pressure coupling was changed from anisotropic to isotropic and the Berendsen barostat[58] was invoked. The crystal subsystem was released, i.e., allowed to move in all three directions, subject to a strong constraining potential ($\lambda = 1.194$). Chains of the melt subsystem, on the other hand, continued under $\lambda = 0.3$, while the temperature was raised to 520 K. Under these conditions, the sandwich system crystallized completely in ~20 ns. Configurations of the system collected in the course of these last 20 ns are shown in Figure 9. In addition, a video of the crystallization is provided in part B of the Supporting Information.

A second set of sandwich simulations employing the constraining potential was undertaken to obtain polycrystalline structures. This second set was started from the configuration obtained after 10.7 ns of equilibration at 440 K and $\lambda = 0.30$ with chains in the crystalline subdomain frozen along the **b** and **c** directions and anisotropic pressure coupling. Instead of removing the freezing from the crystal chains, as described above, we raised the temperature to 460 K, while increasing the coupling parameter on the melt chains to $\lambda = 1.194$. With these settings, we let the simulation evolve for 20 ns. Next, we increased the temperature from 460 to 480 K and allowed the simulation to run for another 20 ns. The abrupt increase in stiffness of the melt chains caused them to form a crystalline nucleus of different orientation in part of the melt subsystem. Reorientation of this nucleus to match the orientation of the preexisting crystalline domain was not possible due to the slow melt dynamics at that temperature. A polycrystalline morphology resulted, which is discussed in section IV.E.

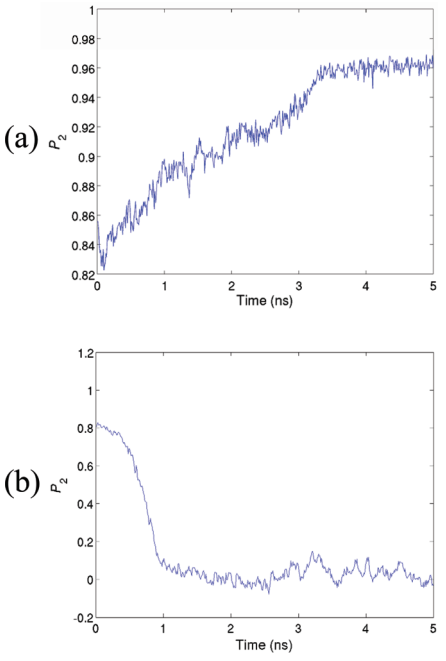

Figure 10. Order parameter P_2 as a function of time for a sandwich system subject to the constraining potential ($\lambda = \lambda_{max} = 0.3$) in both the melt and crystal domains (a) at 757 K; at this temperature, the entire system crystallizes; the order parameter is reaching a plateau value of 0.97 (b) at 758 K; here, the order parameter drops to values around zero, showing that the entire system ends up in the melt (amorphous) state.

D. Prediction of the Melting Point via Gibbs−Duhem Integration. After crystallization of the sandwich system at 520 K following the first set of simulations described in section IV.C, we reduced the constraining potential to $\lambda = 0.3$ everywhere. Upon continuing the MD run, the system remained fully crystalline, indicating that its equilibrium melting point is higher than 520 K at this λ value. Next, we sought to determine the equilibrium melting point of our constrained model under $\lambda = \lambda_{max} = 0.3$. To this end, we took a partially crystalline configuration at 9.5 ns out of the last 20 ns of the 520 K crystallization run described in section IV.C. In this configuration, the melt subdomain was approximately halfway crystallized. The configuration was subjected to *NpT* MD simulations at progressively higher temperatures, above 520 K. It proceeded to crystallize completely at all temperatures below 757 K. On the other hand, at temperatures from 758 K on, melting was found to take place in the same sandwich configuration, quickly converting it entirely into an isotropic phase. The value of $T_m(\lambda = 0.3) = 758 \pm 1$ K was thereby established for the equilibrium melting temperature at $\lambda = 0.3$. This value is, of course, extremely high in relation to the melting point of real iPP because of the strong helix-inducing constraining potential imposed on the system.

The evolution of the structure of the system during crystallization and melting at these two nearby temperatures can be seen characteristically in the orientational order parameter P_2, calculated via the equation

$$P_2(t) = \frac{3}{2}\langle \cos^2 \theta(t) \rangle - \frac{1}{2} \tag{22}$$

where $\cos \theta$ is defined as

$$\cos \theta = \frac{\mathbf{c} \cdot \mathbf{r}_{17}}{|\mathbf{c}||\mathbf{r}_{17}|} \tag{23}$$

Here, $\mathbf{c}$ is the unit cell vector along the axis of the crystal chains and $\mathbf{r}_{17} = \mathbf{r}_{C_{i+6,ich}} - \mathbf{r}_{C_{i,ich}}$ is the vector between any two backbone carbon atoms along the same chain that are three monomer units (six skeletal bonds) apart from each other. Results from calculating the order parameter of the $\lambda = 0.3$ system at 757 and 758 K are shown in Figure 10a,b. The reader should note how much more quickly melting is achieved in relation to freezing. At 758 K, the order parameter drops from an initial value of roughly 0.82, characteristic of the partially ordered initial configuration, to 0 (fully disordered state) in less than 1.5 ns. On the contrary, at 757 K, it takes ~4 ns for the order parameter to rise from the same initial value to 0.97, signaling practically full crystallization.

Having established the equilibrium melting point at $\lambda = \lambda_{max} = 0.3$ (step 1 in the algorithm of section III.F), we now proceed to track the $T_m(\lambda)$ curve down to $\lambda = 0$ and thereby establish the equilibrium melting point of our model 17mer iPP. To this end, we implement steps 2−5 of the algorithm outlined in section III.F. The slope $(\partial T/\partial \lambda)|_{p,eq}$ is estimated via eq 21 from pure liquid and pure crystal simulations at T and λ. The coupling parameter is reduced in small steps, $\Delta\lambda$, and the value of T_m at each new λ is estimated via $\Delta T = (\partial T/\partial \lambda)|_{p,eq}\Delta\lambda$. This procedure is quite sensitive to the value of $\Delta\lambda$ used. Even if (λ, T_m) is a true equilibrium pair, taking a large step $\Delta\lambda$ along the tangent of the $T_m(\lambda)$ curve may result in $(\lambda + \Delta\lambda, T_m + \Delta T)$ no longer corresponding to equilibrium. The more nonlinear the $T_m(\lambda)$ relation is, the more serious the integration error and the smaller the step size $\Delta\lambda$ that has to be used. This discretization error associated with our use of a finite difference estimate for the derivative $(\partial T/\partial \lambda)|_{p,eq}$ requires checking, at least periodically, whether the (λ, T_m) pairs obtained through the Gibbs−Duhem integration indeed constitute equilibrium pairs. This check and revision, if necessary, is accomplished in step 4 of the algorithm outlined in section III.F.

Figure 11 shows results for the $T_m(\lambda)$ curve obtained via Gibbs−Duhem integration/equilibrium sandwich simulation with various $\Delta\lambda$ step sizes. The curve becomes extremely nonlinear at low λ values, as the limit of real iPP is approached. In this region, small $\Delta\lambda$ steps have to be used, and corrections via the equilibrium sandwich simulation become essential. At the same time, sandwich simulations are not easy, as dynamics becomes sluggish at low temperature.

Our best estimate of the equilibrium T_m for the α1 phase of 17mer iPP based on our interaction potential is $T_m = 375$ K. Our experience showed that, for values of λ lower than 0.05, the smaller the step size $\Delta\lambda$ is, the better the estimation of the melting point obtained. Small step sizes, however, increase the computational effort considerably. In view of this, we expect the true melting point of our model to be slightly lower than the one we found here. Our estimate of $T_m = 375$ K compares favorably with the experimental value of $T_m = 348$ K extracted for 17meric iPP based on the experimental data of T_m as a function of molar mass provided in Table 1 of ref 61.

E. Nucleation in the Presence of the Constraining Potential. Our motivation for generating and simulating the sandwich system was to study the secondary crystallization process (crystal growth) because the kinetics of this process is much faster, and the free energy required for new chains to attach to the crystal/melt interface is much lower, making the whole process much more rapid than nucleation. Yet, while trying to crystallize our sandwich system under various conditions, as detailed in sections IV.C and IV.D, we came across interesting phenomena involving the development of a polycrystalline subsystem in place of the preexisting amorphous region. The presence of more than one crystal grains with different orientations, and of boundaries between them, was

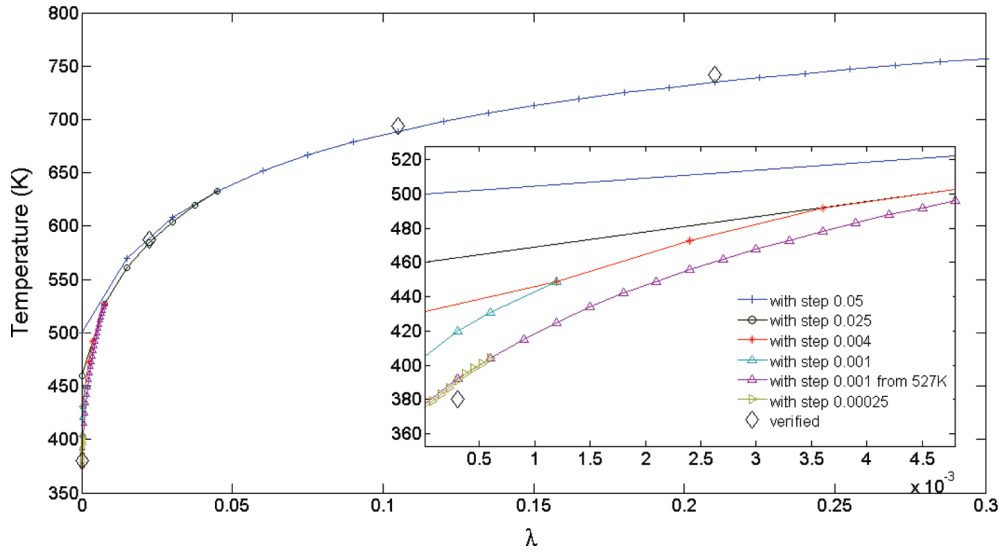

Figure 11. Gibbs−Duhem integration diagram. With the diamond markers are shown results from the sandwich simulations establishing the $T(\lambda)$ at which none of the subdomains of the biphasic system grows at the expense of the other. Lines follow the slopes dictated by eq 21, based on averages computed from single-phase solid and liquid simulations conducted at T and λ. Several lines, corresponding to various discretization steps $\Delta\lambda$, are shown. A very small step size $\Delta\lambda$ is needed to track the sharp turn in the $T(\lambda)$ curve at low λ values. The best estimate of T_m at $\lambda = 0$ is 375 K.

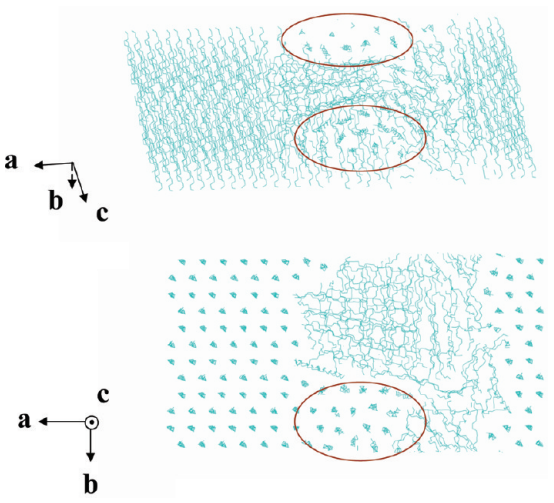

Figure 12. Nucleated system containing crystallites of different orientations, viewed from different sides: Top, along the **b** direction of the originally present crystalline region; Bottom: down the **c** direction of the originally present crystalline region. Encircled are various parts which have crystallized from the melt, viewed down their chain axes. Crystalline domains have emerged, whose orientation is different from the one of the original crystalline subsystem.

obvious. Clearly, crystallization in the presence of our constraining potential did not consist exclusively of growth off of the preexisting lamellar facets but included some homogeneous nucleation in the melt phase. Here we provide a pictorial representation of a polycrystalline structure obtained, showing only the backbone carbon atoms for clarity, in order to enable the reader to distinguish the different crystal layers of helical macromolecules. This structure was formed through the second set of simulations described at the end of section IV.C. The reader can see different views of the final polycrystalline configuration in Figure 12. In addition, a video showing different aspects of this polycrystalline system is provided in part C of the Supporting Information.

The reader may discern the presence of multiple crystal domains even in the first set of sandwich crystallization simulations. In Figure 9a, for example, an ordered nucleus has formed in the top right-hand side of the melt region, close to the interface with the pre-existing crystal. This nucleus, however, has the same orientation as the pre-existing crystal and is quickly engulfed by the growing crystal front. Under the conditions of the first set of simulations, a monodomain ultimately develops (see also video in Supporting Information, part B).

V. Conclusions

In this paper we have used atomistic molecular dynamics simulations to study melting and crystallization of α1 oligomeric isotactic polypropylene. A force field developed in the past for the melt state was shown to have a minimum near the crystallographic structure of the α1 crystal. A way of forming crystalline phases of finite molar mass (in our case, consisting of 17mer chains) from a model crystal of infinite molar mass (with no ends) was designed and implemented. The change in specific volume upon melting and the heat of fusion were estimated from the simulations in good agreement with experiment. A novel method was devised to capture the equilibrium melting temperature, overcoming the great difficulties arising because of slow dynamics in the melt, which hamper crystal nucleation and growth. This method employs a constraining potential which encourages melt chains to adopt helical conformations, such as those encountered in the crystal. Solid−liquid equilibrium is established unequivocally in a sandwich structure consisting of both liquid and crystalline subdomains when the orienting field is strong. This equilibrium is used as a starting point within a Gibbs−Duhem integration scheme that tracks the melting point as a function of the strength of the constraining potential, down to zero constraining potential. The Gibbs−Duhem integration is based on ensemble averages accumulated in the course of single-phase crystal and melt simulations. In parallel, equilibrium simulations of the sandwich structure are used to check the extrapolations of the Gibbs−Duhem integration and correct them, if necessary. An equilibrium melting temperature of 375 K is estimated for the α1 phase of 17meric iPP, in reasonable agreement with existing experimental evidence.[61] The use of an orienting field was found to accelerate not only growth but also homogeneous nucleation in the melt phase, leading to polycrystalline domains in some computer experiments.

Acknowledgment. N.R. thanks Dr. Christos Tzoumanekas for his guidance in FORTRAN coding and Dr. Georgia Evangelia Logotheti for providing her melt configurations and sharing her experience with melt simulations of iPP. Discussions with Stefanos Anogiannakis, Antonia Vykou, Grigorios Megariotis, Dr. Adrien Leygue, Dr. George Boulougouris, and Dr. Dimitrios Tsalikis have been stimulating and informative. Professor George Floudas of the University of Ioannina is thanked for taking care of all administrative aspects of the PENED project with admirable efficiency. Gromacs Developers, and especially Dr. Berk Hess, are thanked for their support and the Ubuntu community for various technical solutions they suggested. Last but not least, Mr. Marco Sant and Dr. George Papadopoulos are thanked for their valuable help in setting up the Beowulf cluster on which the simulations reported in this work have been conducted. This paper is part of the 03ED856 research project, implemented within the framework of the "Reinforcement Programme of Human Research Manpower" (PENED) and cofinanced by National and Community Funds (20% from the Greek Ministry of Development-General Secretariat of Research and Technology and 80% from E.U.-European Social Fund).

Supporting Information Available: (A) Representative results on the structure and thermodynamics of an iPP melt, as predicted with the slightly modified force field used in this work (section III.B), along with the corresponding results obtained with the original force field of ref 52. The latter have already been shown to be in excellent agreement with experiment. (B) A video displaying the crystallization process in a sandwich structure of 17meric iPP in the presence of the constraining potentials, discussed in section IV.C. (C) A polycrystalline configuration, obtained as discussed in sections IV.C and IV.E. This material is available free of charge via the Internet at http://pubs.acs.org.

References and Notes

(1) Reiter, G.; Strobl, G. R. *Progress in Understanding Polymer Crystallization*, 1st ed.; Springer-Verlag: Berlin, 2007; pp 1−508.
(2) Yamamoto, T. *J. Chem. Phys.* **2006**, *125*, 064902.
(3) Meyer, H.; Müller-Plathe, F. *J. Chem. Phys.* **2001**, *115*, 7807–7810.
(4) Meyer, H.; Müller-Plathe, F. *Macromolecules* **2002**, *35*, 1241–1252.
(5) Megariotis, G.; Vyrkou, A.; Leygue, A.; Theodorou, D. N. *Ind. Eng. Chem. Res.*, ASAP.
(6) Muthukumar, M. *Philos. Trans. R. Soc. London A* **2003**, *361*, 539–556.
(7) Doye, J. P. K.; Frenkel, D. *J. Chem. Phys.* **1998**, *109*, 10033.
(8) Yi, P.; Rutledge, G. C. *J. Chem. Phys* . **2009**, *131*, 134902.
(9) Lotz, B. *Eur. Phys. J. E* **2000**, *3*, 185–194.
(10) Brückner, S.; Meille, S. V.; Petraccone, V.; Pirozzi, B. *Prog. Polym. Sci.* **1991**, *16*, 361–404.
(11) IUPAC Commission on Macromolecular Nomenclature, *Pure Appl. Chem.* **1981**, *53*, 733−752.
(12) Yamamoto, T.; Sawada, K *J. Chem. Phys.* **2005**, *123*, 234906.
(13) Esselink, K.; Hilbers, P. A. J.; van Beest, B. W. H. *J. Chem. Phys.* **1994**, *101*, 9033–9041.
(14) Dorset, D. L.; Alamo, R. G.; Mandelkern, L. *Macromolecules* **1992**, *25*, 6284–6288.
(15) Kawai, T. *Kolloid Z. Z. Polym.* **1965**, *201*, 15–20.
(16) Wang, X.; Hou, W.; Zhou, J.; Li, L.; Li, Y.; Chan, Ch. M. *Colloid Polym. Sci.* **2007**, *285*, 449–455.
(17) Yamada, K.; Hikoshata, M.; Toda, A.; Yamazaki, Sh.; Tagashira, K. *Macromolecules* **2003**, *36*, 4790–4801.
(18) Yamada, K.; Hikoshata, M.; Toda, A.; Yamazaki, Sh.; Tagashira, K. *Macromolecules* **2003**, *36*, 4802–4812.
(19) Takahashi, N.; Hikosaka, M.; Yamamoto, T. *Physica B* **1996**, *219&220*, 420–422.
(20) Tsuchiya, Y.; Hasegawa, H.; Iwatsubo, T . *J. Chem. Phys.* **2001**, *114*, 2484–2488.
(21) Sumpter, B. G.; Noid, D. W.; Wunderlich, B.; Cheng, S. Z. D. *Macromolecules* **1990**, *23*, 4671–4677.
(22) Goldfarb, L. *Makromol. Chem.* **1978**, *179*, 2297–2303.
(23) Lotz, B. *Polymer* **1998**, *39*, 4561–4567.
(24) Naiki, M.; Kikkawa, T.; Endo, Y.; Nozaki, K.; Yamamoto, T.; Hara., T. *Polymer* **2001**, *42*, 5471–5477.
(25) Wang, J.; Dou, Q. *Polym. Int.* **2008**, *57*, 233–239.
(26) Yuan, Q.; Rajan, V. G.; Misra, R. D. K. *Mater. Sci. Eng., B* **2008**, *153*, 88–95.
(27) Medellin-Rodriguez, F. J.; Mata-Padilla, M.; Sanchez-Valdes, S.; Vega-Diaz, S.; Davalos-Montoya, O. *J. Polym. Sci., Part B: Polym. Phys.* **2008**, *46*, 2188–2200.
(28) Iijima, M.; Strobl, G. *Macromolecules* **2000**, *33*, 5204–5214.
(29) Androsch, R.; Wunderlich, B. *Macromolecules* **2001**, *34*, 5950–5960.
(30) Kavassalis, T. A.; Sundararajan, P. R. *Macromolecules* **1993**, *26*, 4144–4150.
(31) Lacevic, N.; Fried, L. E.; Gee, R. H. *J. Chem. Phys.* **2008**, *128*, 014903.
(32) Zhang, X.-B.; Li, Z.-S.; Lu, Z.-Y.; Sun, C.-S. *Polymer* **2002**, *43*, 3223–3227.
(33) Ko, M. J.; Waheed, N.; Lavine, M. S.; Rutledge, G. C. *J. Chem. Phys.* **2008**, *121*, 2823–2832.
(34) Lavine, M. S.; Waheed, N.; Rutledge, G. C. *Polymer* **2003**, *44*, 1771–1779.
(35) Yamamoto, T. *J. Chem. Phys.* **2008**, *129*, 184903.
(36) Yamamoto, T.; Nozaki, K.; Yamagushi, A.; Urakami, N. *J. Chem. Phys.* **2007**, *127*, 154704.
(37) Waheed, N.; Lavine, M. S.; Rutledge, G. C. *J. Chem. Phys.* **2001**, *116*, 2301–2309.
(38) Waheed, N.; Ko, M. J.; Rutledge, G. C. *Polymer* **2005**, *46*, 8689–8702.
(39) Takeuchi, H. *J. Chem. Phys.* **1998**, *109*, 5614.
(40) Kuppa, V. K.; in't Veld, P. J.; Rutledge, G. C. *Macromolecules* **2007**, *40*, 5187–5195.
(41) Yamamoto, T. *Polymer* **2009**, *50*, 1975–1985.
(42) Haliloğlu, T.; Mattice, W. L. *J. Chem. Phys.* **1998**, *108*, 6989.
(43) Gliguem., H.; Ghorbel, D.; Lopez, C.; Michon, C.; Ollivon, M.; Lesieur, P. *J. Agric. Food. Chem.* **2009**, *57*, 3195–3203.
(44) Svang-Ariyaskul, A.; Koros, W. J.; Rousseau, R. W. *Chem. Eng. Sci.* **2009**, *64*, 1980–1984.
(45) Wang, W.; Wei, L.; Yang, A.; He, T.; Yuen, K. Y.; Chen, C.; Rao, Z. *Acta Crystallogr., Sect. F: Struct. Biol. Cryst. Commun.* **2009**, *65*, 526–528.
(46) Bombelli, F. B.; Betti, F.; Gambinossi, F.; Caminati, G.; Brown, T.; Baglioni, P.; Berti, D. *Soft Matter* **2009**, *5*, 1639–1645.
(47) Strobl, G. *The Physics of Polymers*, 3rd ed.; Springer-Verlag: Germany, 2007; pp 165−222.
(48) Natta, G.; Corradini, P. *Nuovo Cimento Suppl.* **1960**, *15*, 40.
(49) Immirzi, A.; Iannelli, P. *Macromolecules* **1988**, *21*, 768–773.
(50) Hikosata, M.; Seto, T. *Polym. J.* **1973**, *5*, 111–127.
(51) Antoniadis, J., St.; Samara, C. T.; Theodorou, D. N. *Macromolecules* **1998**, *31*, 7944–7952.
(52) Logotheti, G. E.; Theodorou, D. N. *Macromolecules* **2007**, *40*, 2235–2245.
(53) Theodorou, D. N.; Suter, U. W. *Macromolecules* **1985**, *18*, 1467–1478.
(54) Sylvester, M. F.; Yip, S.; Argon, A. S. In *Computer Simulation of Polymers*, 1st ed.; Roe, R. J., Ed.; Prentice-Hall: Englewood Cliffs, NJ, 1991; pp 105−121.
(55) Antoniadis, J., St.; Samara, C. T.; Theodorou, D. N. *Macromolecules* **1999**, *32*, 8635–8644.
(56) Hess, B.; Kutzner, C.; van der Spoel, D.; Lindahl, E. *J. Chem. Theory Comput.* **2008**, *4*, 435–447.
(57) Hoover, W. G. *Phys. Rev. A* **1986**, *34*, 2499.
(58) Berendsen, H. J. C.; Postma, J. P. M.; Van Gunsteren, W. F.; DiNola, A.; Haak, J. R. *J. Chem. Phys.* **1984**, *81*, 3684–3690.
(59) Parrinello, M.; Rahman, A. *J. Appl. Phys.* **1981**, *52*, 7182–7190.
(60) Graessley, W. W.; Edwards, S. F. *Polymer* **1981**, *22*, 1329–1334.
(61) Pino, P.; Cioni, P.; Wei, J. *J. Am. Chem. Soc.* **1987**, *109*, 6189–6191.
(62) Goldfarb, L. *Makromol. Chem.* **1978**, *179*, 2297–2303.
(63) Wang, J.; Dou, Q. *Polym. Int.* **2008**, *57*, 233–239.
(64) Francisco, J.; Rodriguez, M.; Mata-Padilla, M.; Sanchez-Valdes, S.; Vega-Diaz, S.; Davalos-Montoya, O. *J. Polym. Sci., Part B: Polym. Phys.* **2008**, *46*, 2188–2200.
(65) Siavosh-Haghighi, A.; Thompson, D. L. *J. Phys. Chem. C* **2007**, *111*, 7980–7985.
(66) Gulam Razul, M. S.; Hendry, J. G.; Kusalik, P. G. *J. Chem. Phys.* **2005**, *123*, 204722.
(67) Vatamanu, J.; Kusalik, P. G. *J. Chem. Phys.* **2007**, *126*, 124703.
(68) Fernandez, R. G.; Abascal, J. L. F.; Vega, C. *J. Chem. Phys.* **2006**, *124*, 144506.

(69) Wang, K.; Wu, J.; Zeng, H. *Eur. Polym. J.* **2003**, *39*, 1647–1652.
(70) Di Lorenzo, M. L.; Cimmino, S.; Silvestre, Cl. *Macromolecules* **2000**, *33*, 3828–3832.
(71) Joseph, A.; Koch, T.; Seidler, S.; Thomas, S.; Joseph, K. *J. Appl. Polym. Sci.* **2008**, *109*, 1714–1721.
(72) Gitsas, A.; Floudas, G. *Macromolecules* **2008**, *41*, 9423–9429.
(73) Sadiku, E. R. *Acta Polym.* **1990**, *41*, 246–251.
(74) Kofke, D. A. *Mol. Phys.* **1993**, *78*, 1331.
(75) Kofke, D. A. *J. Chem. Phys.* **1993**, *98*, 4149.
(76) Allen, M . P.; Tildesley, D. J. *Computer Simulation of Liquids*; Oxford University Press: Oxford, 1987; pp 33−70.
(77) Isasi, J. R.; Alamo, R. G.; Mandelkern, L. *J. Polym. Sci., Part B: Polym. Phys.* **1997**, *35*, 2945–2949.
(78) Sato, Y.; Yamasaki, Y.; Takishima, S.; Masuoka, H. *J. Appl. Polym. Sci.* **1997**, *66*, 141–150.
(79) Chang, C.; Yi, X. S.; Asai, S.; Sumita, M. *J. Mater. Sci.* **2000**, *35*, 673–683.
(80) Fatou, J. G. *Eur. Polym. J.* **1971**, *7*, 1057–1064.
(81) Gee, D. R.; Melia, T. P. *Makromol. Chem.* **1970**, *132*, 195–201.